Structural, optical and magnetic properties of Ni-doped ZnO micro-rods grown by the spray pyrolysis method

S. Yılmaz [a,b] , E. McGlynn [b], E. Bacaksız [a*], J. Cullen [b], R.K. Chellappan [c]

[a] Department of Physics, Faculty of Sciences, Karadeniz Technical University, 61080 Trabzon, Turkey

[b] School of Physical Sciences and National Centre for Plasma Science and Technology, Dublin City University, Glasnevin, Dublin 9, Ireland

[c] School of Physical Sciences and National Centre for Sensor Research, Dublin City University, Glasnevin, Dublin 9, Ireland

[*] Corresponding author: Tel: +90 462 377 25 45 fax: +90 462 325 31 95
e-mail:eminb@ktu.edu.tr

Abstract

Undoped and Ni-doped ZnO micro-rod arrays were successfully synthesized by the spray pyrolysis method on glass substrates. Analysis of the samples with x-ray diffraction and scanning electron microscopy showed that these micro-rod arrays had a polycrystalline wurtzite structure with a highly *c*-axis preferred orientation. Photoluminescence studies at both 300 K and 10 K show that the incorporation of nickel leads to a relative increase in the visible blue light band intensity. Magnetic measurements indicated that Ni-doped ZnO samples exhibit ferromagnetic behavior at room temperature, which is possibly related to the presence of point defects.

Keywords: Ni:ZnO, Micro rod; Photoluminescence; Ferromagnetism

1. Introduction

Diluted magnetic semiconductor (DMS) is a type of semiconductor where a fraction of the host cations can be substitutionally replaced by magnetic ions and this class of semiconductors has attracted much attention because of the potential use of both the charge and spin of electrons for spintronic devices such as spin-valve transistors [1], spin light-emitting diodes [2], logic devices [3] and nonvolatile memory [4]. Such spin-based devices are multifunctional and possess higher speed, greater efficiency, lower electrical power consumption and better stability. The basic requirement for these practical applications is to achieve a Curie temperature (T_c) well above room temperature. ZnO, a wide band gap (3.37 eV) semiconductor with a large exciton binding energy (60 meV), is gaining much interest for various applications such as UV light emitters [5], piezoelectric devices [6], gas sensors [7] and solar cells [8]. In addition to these, ZnO has been also one of the promising candidates for DMS since Dietl et al. predicted that room-temperature ferromagnetism could be created by substituting Mn ions into *p*-type wide-band gap semiconductors such as GaN and ZnO [9] and the theoretical ab initio calculations of Sato et al., based on the local density approximation, which showed that ZnO doped with several 3d transition metal ions such as V, Cr, Fe, Co and Ni may exhibit ferromagnetic ordering with T_c above room temperature [10]. There are a range of experimental studies focusing on Ni-doped ZnO where diverse magnetic properties have been observed. However, these studies indicate that ferromagnetism strongly depends on the methods and conditions used in their preparation. For example, Liu et al. reported room temperature ferromagnetism in Ni-doped ZnO thin films grown by pulsed-laser deposition [11]; above 30 K superparamagnetic behavior was obtained by Bodker et al. [12]. Yu et al. observed room temperature ferromagnetism in ZnO films doped with 1%, 3%, and 5% of Ni [13]. On the other hand, Jin et al. found no indication of ferromagnetism in $Zn_{1-x}Ni_xO$ (x=0 to 0.2) down to 2 K [14]. Furthermore, paramagnetism was attained by Yin et al. in $Zn_{0.86}Ni_{0.14}O$

samples down to 5 K [15]. Although there are many experimental reports on ZnO based DMS exhibiting room temperature ferromagnetism, the origin of the ferromagnetism is still controversial [16]. Early studies explained that a free carrier mediated mechanism was responsible for the ferromagnetic behavior [10]. However, more recent studies proposed that defects like oxygen vacancies give rise to ferromagnetic ordering in oxide based DMS [17].

A considerable research effort has recently been focused on studying transition metal-doped one-dimensional (1D) ZnO nano/microstructures (such as wires, rods, and tubes) due to their potential use in producing nano/microscale spintronic devices [18]. Among the transition metal ions, Ni is the most efficient doping elements to improve and tune the optical, electrical and magnetic properties of ZnO materials [19]. Ni is also very much unstable metal in the ZnO matrix, hence it has the tendency to form clusters of metallic Ni or NiO [20]. There are various methods to fabricate one-dimensional transition metal-doped ZnO materials. These techniques include chemical vapor deposition [21], hydrothermal method [22], thermal evaporation [23] and spray pyrolysis technique [24]. Among these, the spray pyrolysis is especially suitable, since it has proved to be a simple and inexpensive method, particularly useful for large area applications. Furthermore, there is much less research on the use of spray pyrolysis method for the growth of one-dimensional transition metal-doped ZnO materials in the literature and it is our intention to undertake a novel and necessary study of the use and potential of this growth method to grow ZnO-based DMS. In this communication, we present data on ZnO micro-rod arrays synthesized via spray pyrolysis on glass substrates and specifically we study the effects of the increase of Ni-doping concentration on ZnO samples using x-ray diffraction (XRD), scanning electron microscopy (SEM), photoluminescence (PL) and magnetic measurements. We discuss the relationship between the optical and magnetic properties with a view to explaining the origin of observed room temperature ferromagnetism in our Ni-doped ZnO micro-rod samples.

2. Experimental details

$Zn_{1-x}Ni_xO$ micro-rod arrays with nominal molar fraction (x) values of 0.00, 0.02, 0.04 and 0.06 were prepared by the spray pyrolysis method in an air atmosphere. The experimental setup and other experimental procedures are explained in more detail elsewhere [24]. The initial stock solution was prepared from zinc chloride ($ZnCl_2$) at 0.1 M concentration in deionized water. Doping was achieved by the addition of $NiCl_2.6H_2O$ (0.1 M) to the stock solution, which was then sprayed on the glass substrate. The growth was performed with a spray rate of about 5 ml/min and a growth rate of ~ 50 nm/min. Prior to growth, glass substrates were cleaned in ethanol and then dried in vacuum. During the growth, the substrates were rotated with a speed of 10 revolutions per minute and the substrate was held at a temperature of 550 °C. X-ray diffraction (XRD) data of the samples in θ-2θ mode were taken using a Bruker AXS D8 advance texture diffractometer with CuK_α radiation over the range 2θ=20–60° with a step of 0.01° at room temperature. The surface morphology and bulk composition were studied with a JEOL JSM-6400 SEM equipped with EDS (Energy Dispersive X-ray Spectroscopy). An acceleration voltage of 20 kV was used in all cases for this study. Photoluminescence (PL) measurements were performed at both 10 K and 300 K. A SPEX 1704 monochromator with a closed cycle cryostat Janis SHI-950-5 was used. PL spectra were excited with both the 325 nm line of a He–Cd laser and 532 nm line of a Nd:YAG operating at 200 mW. Magnetization measurements of the samples as a function of magnetic field and temperature were carried out using a Quantum Design Physical Property Measurement System (PPMS) system with a vibration sample magnetometer module.

3. Results and discussion

The structural properties of undoped ZnO and Ni-doped ZnO micro-rod arrays produced by the spray pyrolysis method were investigated by XRD and the results for all samples are shown in Fig. 1(a)-(d). The XRD patterns of these samples are in good agreement

with the JCPDS standard (No. 36-1451) data of wurtzite (hexagonal) ZnO powder. It was seen that undoped and Ni-doped ZnO samples exhibit peaks corresponding to (100), (002), (101) and (102) planes, with the (002) peak showing the highest intensity in all cases, implying that all the samples have a hexagonal crystal structure with a preferred orientation with the substrate normal parallel to the normal of the ZnO (002) plane. However, when the nominal concentration of Ni increased, a NiO peak (200) appears at 43.14° and 43.11° for 4 at.% and 6 at.% Ni-doped ZnO samples, respectively, meaning that a NiO secondary phase was introduced to the these samples due to the limited solid solubility of Ni in ZnO host matrix. El-Hilo et al. found that Ni can dissolve up to 1 at.% into ZnO matrix, however, as the Ni concentration increased to 4.3 at.%, a NiO secondary phase was detected for Ni-doped ZnO nanocrystal samples [25]. Additionally, Singh et al. produced Ni-doped ZnO polycrystalline samples by sol-gel technique and obtained that NiO impurity peaks observed at 2.5 at.% Ni content [26]. The lattice constant c of undoped ZnO was calculated from the plane of ZnO (002) and found to be 5.21 Å. With the increase of the Ni doping, the lattice parameter value has not changed significantly because of near same ionic radius of Zn^{2+} and Ni^{2+}, implying Ni doping has not altered the ZnO crystal structure.

Chemical compositions of undoped and Ni-doped ZnO microrods were investigated by EDS and listed in Table 1. Table 1 indicates that all the samples are composed of Zn, O or Ni, demonstrating an increase in actual Ni concentration with the increase of nominal Ni-doping in ZnO micro-rods. Table 1 also shows that actual atomic percentage ratio of Ni is less than the nominal composition in the solution. The difference between the actual and the nominal Ni concentration is probably due to the dilution of Ni ions in the ZnO host matrix. In addition, compared to undoped ZnO, it was found that the Ni-doped ZnO microrods were slightly zinc deficient and oxygen rich, beyond that expected for Zn replacement by Ni. Similar results were obtained by Wang et al. for Cu-doped ZnO nanoparticle sheets [27].

SEM surface micrographs for the samples are shown in Fig. 2 and reveal that undoped, 1.2 at.%, 2.6 at.% and 4.4 at.% Ni-doped ZnO samples have hexagonal shaped microrods with sub-micron diameters. Compared to the undoped ZnO, it was observed that the morphology of the microrods exhibits no essential difference with the increase of Ni doping. However, there is some variation in microrod diameter within individual samples as seen in Fig. 2. Based on the data from XRD pattern in Fig.1 and the cross-section image of undoped ZnO sample as illustrated in the inset of Fig. 2(a), the hexagonal rods with a height of ~ 7 μm were found to be regular and almost perpendicular to the substrate, indicating that undoped and Ni-doped ZnO rods preferentially grow along the (002) plane.

The effects of Ni-doping on optical emission and defect formation were investigated by PL measurements. Room temperature PL emission spectra of undoped and Ni-doped ZnO samples grown on glass substrates are shown in Fig. 3. As seen from Fig. 3, undoped ZnO exhibits only a UV peak, which was related to the recombination of the free excitons with both no-phonon and LO phonon replica contributions [28]. However, all the Ni-doped ZnO samples display two distinct emission peaks: a weak one in the UV region and another broad one in the range of 390-520 nm of visible blue light (VBL) region which is usually attributed to intrinsic defects such as zinc vacancy (V_{Zn}), interstitial zinc (Zn_i), singly negatively charged Zn vacancy (V_{Zn}^-) and oxygen vacancy (V_o) [29-31]. With the increase of nickel doping level, relative peak intensity of VBL increased gradually, suggesting an increase of the concentrations of the responsible point defects mentioned above. Inset of Fig. 3 shows the results of multiple Gaussian fittings of the room temperature PL spectra for 4.4 at.% Ni-doped ZnO sample. The weak UV luminescence peak located at ~ 386 nm, corresponding to a photon energy of ~ 3.21 eV, is related to near band edge emission. Other peaks are found in the visible blue spectral region via the fitting of the entire emission at energies of 3.00 eV,

2.84 eV, 2.67 eV and 2.55 eV which may correspond to V_{Zn}, Zn_i, V_{Zn}^- and V_o, respectively, which are in good agreement with other studies in the literature [32,33].

Fig. 4 shows low temperature PL spectra measured at 10 K of undoped and Ni-doped ZnO microrods. The UV peaks of all the samples are located at 3.361 eV and are ascribed to the near band edge (NBE) emission of excitons bound to donors (D^0X, members of the so-called I lines) [34]. The energies of these peaks are identical within about 5 meV for all samples, indicating that the dominant donor bound exciton emission energy is unaffected by the Ni incorporation. This D^0X emission is observed at a constant energy below the band gap and thus indicates that the band gaps at low temperatures in all samples are identical. The undoped ZnO sample also exhibits three peaks located at 3.287 eV, 3.219 eV and 3.146 eV, respectively, in the band edge region. These peaks correspond closely to the first three longitudinal-optical (LO) phonon replicas of the D^0X emission, with a spacing close to the LO phonon energy of ~ 72 meV [35]. After doping the ZnO microrods with Ni, these peaks reduce dramatically, due to a reduction in the relative intensity of the near band edge emission, as shown in Fig. 4. Similar to the 300 K data, in the visible blue light region, Ni-doped samples display a defect-related visible luminescence band which increased in relative intensity, compared to the UV peak, with increased Ni-doping level. Thus, the PL data of both 300 K and 10 K show evidence for an increase in optically active deep level defects with increased Ni-doping level. However, at longer wavelengths, especially 1.2 at.% and 2.6 at.% Ni-doped ZnO samples exhibit broad red luminescence in the range of 600-800 nm. The appearance of this luminescence can be explained as follows: As compared to the undoped sample, low concentration of Ni doping triggered to form O_i defects in this sample, which is good agreement with low temperature PL results as can be seen in Fig. 4. With the increase of Ni doping to 2.6 at.%, O_i defects continued to increase. However, after 4.4 at.% Ni doping, ZnO host matrix had more O_i defects and hence there may be some recombination between O_i

and V_o defects which conclude to reduce the concentrations of O_i defects, which lead to the decrease of the red luminescence band originating from O_i defects [36].

The inset of Fig. 4 shows PL data for 2.6 at.% Ni-doped ZnO sample, measured with Nd:YAG laser excitation (532 nm) at 10 K, between 550 nm and 950 nm. The peak, on the left side of the spectrum, corresponding to energy ~ 2.08 eV may be related to the oxygen interstitial (O_i) defects [37]. On the other hand, the peak corresponding to energy ~ 1.78 eV is probably related to the spin orbit split $^3T_1(P) \rightarrow {}^3T_1(F)$ ligand field transition of substitutional $Ni^{2+}(3d^8)$ ions in a tetrahedral crystal field [38-40].

The magnetization versus magnetic field (M-H) curves measured at 300 K for undoped, 1.2 at.%, 2.6 at.% and 4.4 at.% Ni-doped ZnO micro-rods is shown in Fig. 5. The diamagnetic signal from the glass substrate was subtracted in these measurements. It was observed that undoped ZnO sample showed diamagnetic behavior whereas all three Ni-doped samples exhibited clear ferromagnetic behavior at room temperature. Similar diamagnetic behavior was obtained by Liu et al. for pure ZnO in In-doped ZnO nanowires grown by vapor phase transport process [41]. The coercive field (H_c) and the remnant magnetization (M_r) of 1.2 at.% Ni-doped ZnO micro-rods are found to be ~ 143 Oe and ~ 0.44 emu/cm^3, respectively. H_c and M_r values firstly increased up to ~ 190 Oe, ~ 0.57 emu/cm^3 for 2.6 at.% Ni-doped ZnO. However, these values then decreased to ~ 187 Oe, ~ 0.34 emu/cm^3 for 4.4 at.% Ni-doped ZnO sample. The observed ferromagnetic behaviour of 1.2 at.% and 2.6 at.% Ni-doped ZnO samples could be ascribed to the Ni ions substituting for Zn lattice ions [42]. However, with the further increase of the Ni doping to 4.4 at.%, the NiO peak was seen clearly from XRD patterns, suggesting that higher Ni concentration in ZnO lead to the formation of NiO phase which result in the decline of the ferromagnetism due to the antiferromagnetic nature of NiO. The antiferromagnetic interaction between neighboring Ni–Ni ions suppressed the ferromagnetism at higher doping concentration of Ni, concluding the

decrease of the ferromagnetism. On the other hand, some Ni ions are still incorporated into the ZnO [43].

It was proposed that oxygen vacancies can cause a marked change in the band structure of host semiconductors and make an important contribution to the ferromagnetism [44]. The formation of bound magnetic polarons (BMPs), which include electrons locally trapped by oxygen vacancy, with the trapped electron occupying an orbital overlapping with the d shells of transition-metal (TM) neighbors, has also been suggested to explain the origin of ferromagnetism [45]. In addition to these theoretical studies, several experimental groups have reported that the intrinsic defects play crucial roles in the ferromagnetism of TM-doped ZnO. For example, Yan et al. pointed out that oxygen vacancies play an important role in the appearance of room temperature ferromagnetism for Mn-doped ZnO nanorods [46]. Liu et al. [32] indicated that point defects such as Zn_i or V_{Zn} are responsible for ferromagnetism in Cr:ZnO samples and Hong et al. [47] have pointed out that the magnetization in their Cr:ZnO films is related to oxygen vacancies (V_o). Furthermore, Liu et al. [48] suggested that two key factors lead to the appearance of ferromagnetism in TM-doped ZnO nanocrystals: one is the increase of the number of defects and oxygen vacancies, the other is the exchange interactions between the TM ions and the O ion spin moment.

The observed ferromagnetism of our Ni-doped ZnO samples could originate from a number of possible sources. The first possibility is metallic Ni, which is a well known ferromagnetic material. However, XRD results clearly indicate no metallic Ni in the Ni-doped ZnO samples and PL results also show that Ni ions are in the divalent state. In addition, whereas NiO was observed from the XRD measurements of samples with Ni concentrations of 2.6 at.% and 4.4 at.%, it is also an unlikely candidate because of its antiferromagnetism with a Neel temperature of 520 K [49]. We can conclude that the observed ferromagnetism at room temperature is an intrinsic property of Ni-doped ZnO micro-rods. As discussed

previously, PL spectra can provide information on optically active deep level defects in the Ni-doped ZnO microrods. According to PL results, compared to the undoped sample, Ni-doped ZnO samples show evidence of a considerable population of point defects such as oxygen vacancies, zinc vacancies and zinc interstitials which may play significant roles e.g. by binding the spins of magnetic ions to form bound magnetic polarons, consistent with the hypothesis that such defects may be the origin of the observed room temperature ferromagnetism [32, 33, 45].

Magnetization versus temperature (M–T) curves were also measured in the temperature range of 5-300 K and are plotted in Fig. 6. As seen from this figure, the temperature dependence of the magnetization of the 4.4 at.% Ni-doped ZnO sample is linear at high temperatures. At lower temperatures it displays a steep rise with pronounced concave curvature but without showing any distinct magnetic phase transition. Based on these data we can conclude that the Curie temperature for this sample is well above room temperature, but it is hard to determine the exact value, since the value of the Curie temperature is rather high, exceeding the range of our measurements. Quite a number of works in the literature have shown that Ni-doped ZnO shows ferromagnetism at Curie temperatures above room temperature and our data is consistent with these reports [16, 50].

4. Conclusions

Based on the structural, optical and magnetic measurements of our samples the following main points emerge: (i) all the samples exhibit hexagonal structure with a strong (002) preferred orientation and from the XRD results, a small quantity of NiO phase is also present except for 1.2 at.% Ni-doped ZnO sample; (ii) Ni incorporation did not significantly change the texture or the morphology; (iii) compared to the undoped ZnO, the number of optically active deep level defects increased for Ni-doped ZnO microrod samples; (iv) magnetic

measurements indicated that all the Ni-doped ZnO samples show clear ferromagnetic behavior at room temperature and the origin of the observed room temperature ferromagnetism is most likely due to the intrinsic defects.

Acknowledgement: This work was supported by the research fund of Karadeniz Technical University, Trabzon, Turkey, under contract no. 2008.111.001.9. The author (SY) also gratefully acknowledges the support of the Council of Turkish Higher Education in the form of a fellowship to support extended visits to foreign institutions.

Figure Captions

Fig. 1. XRD patterns of (a) undoped, (b) 1.2 at.% Ni-, (c) 2.6 at.% Ni- and (d) 4.4 at.% Ni-doped ZnO micro-rod arrays.

Fig. 2. SEM images of (a) undoped, (b) 1.2 at.% Ni-, (c) 2.6 at.% Ni-, (d) 4.4 at.% Ni-doped and (e) a cross-section image of the undoped ZnO micro-rod arrays.

Fig. 3. Room temperature PL spectra of undoped, 1.2 at.% Ni-, 2.6 at.% Ni- and 4.4 at.% Ni-doped ZnO micro-rod arrays as recorded at 10 K. Inset shows an enlarged visible photon energy region of 2.2 - 3.4 eV with the Gaussian model fitting.

Fig. 4. Low temperature PL spectra of undoped, 1.2 at.% Ni-, 2.6 at.% Ni- and 4.4 at.% Ni-doped ZnO micro-rod arrays as measured at 10 K. Inset shows PL data in the range of 550 - 950 nm, obtained with Nd:YAG laser (532 nm) at 10 K for 2.6 at.% Ni-doped ZnO sample.

Fig. 5. Room temperature M-H curves of 1.2 at.% Ni-, 2.6 at.% Ni- and 4.4 at.% Ni-doped ZnO micro-rod arrays.

Fig. 6. Temperature dependence of magnetization of 4.4 at.% Ni-doped ZnO micro-rod arrays.

Table Captions

Table 1. Actual atomic concentrations of Zn, O or Ni in undoped and nominally 2 at.% Ni-, 4 at.% Ni- and 6 at.% Ni-doped ZnO microrods

References

[1] J.K. Furdyna, J. Appl. Phys., 64 (1988) R29.

[2] S.J. Pearton, C.R. Abernathy, M.E. Overberg, G.T. Thaler, D.P. Norton, N. Theodoropoulou, A.F. Hebard, Y.D. Park, F. Ren, J. Kim, L.A. Boatner, J. Appl. Phys., 93 (2003) 1.

[3] S.D. Sarma, American Scientist, 89 (2001) 516.

[4] S.A. Wolf, D.D. Awschalom, R.A. Buhrman, J.M. Daughton, S. von Molnar, M.L. Roukes, A.Y. Chtchelkanova, D. Treger, Science, 294 (2001) 1488.

[5] S.H. Jeong, B.S. Kim, B.T. Lee, Appl. Phys. Lett., 82 (2003) 2625.

[6] X.Y. Kong, Z.L. Wang, Nano Lett., 3 (2003) 1625.

[7] O.I. Lupan, S.T. Shishiyanu, T.S. Shishiyanu, Superlattice Microst., 42 (2007) 375.

[8] D.-I. Suh, S.-Y. Lee, T.-H. Kim, J.-M. Chun, E.-K. Suh, O.-B. Yang, S.-K. Lee, Chem. Phys. Lett. 442 (2007) 348.

[9] T. Dietl, H. Ohno, F. Matsukura, J. Cibert, D. Ferrand, Science, 287 (2000) 1019.

[10] K. Sato, H. Katayama-Yoshida, Jpn. J. Appl. Phys., 39 (2000) L555.

[11] X.X. Liu, F.T. Lin, L.L. Sun, W.J. Cheng, X.M. Ma, W.Z. Shi, Appl. Phys. Lett., 88 (2006) 062508.

[12] F. Bodker, M.F. Hansen, C.B. Koch, S. Morup, J. Magn. Magn. Mater., 221 (2000) 32.

[13] W. Yu, L.H. Yang, X.Y. Teng, J.C. Zhang, Z.C. Zhang, L. Zhang, G.S. Fu, J. Appl. Phys., 103 (2008) 093901.

[14] Z. Jin, T. Fukumura, M. Kawasaki, K. Ando, H. Saito, T. Sekiguchi, Y.Z. Yoo, M. Murakami, Y. Matsumoto, T. Hasegawa, H. Koinuma, Appl. Phys. Lett., 78 (2001) 3824.

[15] Z.G. Yin, N.F. Chen, F. Yang, S.L. Song, C.L. Chai, J. Zhong, H.J. Qian, K. Ibrahim, Solid State Commun., 135 (2005) 430.

[16] B.B. Lia, X.Q. Xiu, R. Zhang, Z.K. Tao, L. Chen, Z.L. Xie, Y.D. Zhenga, Z. Xie, Mat. Sci. Semicon. Proc., 9 (2006) 141.

[17] J.M.D. Coey, A.P. Douvalis, C.B. Fitzgerald, M. Venkatesan, Appl. Phys. Lett., 84 (2004) 1332.

[18] H. Ohno, Science, 281 (1998) 951.

[19] H. Saeki, H. Tabata, T. Kawai, Solid State Commun., 120 (2001) 439.

[20] L.-N. Tong, T. Cheng, H.-B. Han, J.-L. Hu, X.-M. He, Y. Tong, C.M. Schneider, J. Appl. Phys., 108 (2010) 023906.

[21] J.J. Liu, M.H. Yu, W.L. Zhou, J. Appl. Phys., 99 (2006) 08M119.

[22] Y. Zuo, S. Ge, Z. Chen, L. Zhang, X. Zhou, S. Yan, J. Alloy and Compd., 470 (2009) 47.

[23] K.-H. Zheng, Z. Liu, J. Liu, L.-J Hu, D.-W. Wang, C.-Y. Chen, L.-F. Sun, Chin. Phys. B, 19 (2010) 026101.

[24] S. Yılmaz, M. Parlak, Ş. Özcan, M. Altunbaş, E. McGlynn, E. Bacaksız, Appl. Surf. Sci., 257 (2011) 9293.

[25] M. El-Hilo, A.A.Dakhel, A.Y.Ali-Mohamed, J. Magn. Magn. Mater., 321 (2009) 2279.

[26] S. Singh, N. Rama, M.S.R. Rao, Appl. Phys. Lett., 88 (2006) 222111.

[27] R.C. Wang, H.Y. Lin, Mater. Chem. Phys., 125 (2011) 263.

[28] D.C. Reynolds, D.C. Look, B. Jobai, C.W. Litton, T.C. Collins, W. Harsch, G. Cantwell, Phys. Rev. B, 57 (1998) 12151.

[29] S.A. Studenikin, N. Golego, M. Cocivera, J. Appl. Phys., 84 (1998) 2287.

[30] Y.W. Heo, D.P. Norton, S.J. Pearton, J. Appl. Phys., 98 (2005) 073502.

[31] H. Usui, J. Phys. Chem. C, 111 (2007) 9060.

[32] H. Liu, X. Zhang, L. Li, Y.X. Wang, K.H. Gao, Z.Q. Li, R.K. Zheng, S.P. Ringer, B. Zhang, X.X. Zhang, Appl. Phys. Lett., 91 (2007) 072511.

[33] X. Zhang, W.H. Wang, L.Y. Li, Y.H. Cheng, X.G. Luo, H. Liu, Z.Q. Li, R.K. Zheng, S.P. Ringer, EPL, 84 (2008) 27005.

[34] B.K. Meyer, H. Alves, D.M. Hofmann, W. Kriegseis, D. Forster, F. Bertram, J. Christen, A. Hoffmann, M. Straßburg, M. Dworzak, U. Haboeck, A.V. Rodina, Phys. Status Solidi b, 241 (2004) 231.

[35] D.C. Reynolds, D.C. Look, B. Jogai, R.L. Jones, C.W. Litton, W. Harsch, G. Cantwell, J. Lumin., 82 (1999) 173.

[36] Z.Q. Chen, M. Maekawa, A. Kawasuso, S. Sakai, H. Naramoto, J. Appl. Phys., 99 (2006) 093507.

[37] S.A. Studenikin, N. Golego, M. Cocivera, J. Appl. Phys., 84 (1998) 2287.

[38] H.A. Weakliem, J. Chem. Phys., 36 (1962) 2117.

[39] C. Ronning, C. Borschel, S. Geburt, R. Niepelt, Mater. Sci. Eng. R, 70 (2010) 30.

[40] R.S. Anderson, Phys. Rev., 164 (1967) 398.

[41] K.W. Liu, M. Sakurai, M. Aono, J. Appl. Phys. 108 (2010) 043516.

[42] X.X. Lin, Y.F. Zhu, W.Z. Shen, J. Phys. Chem. C, 113 (2009) 1812.

[43] C.J. Cong, J.H. Hong, Q.Y. Liu, L. Liao, K.L. Zhang, Solid State Commun., 138 (2006) 511.

[44] L.W. Guo, D.L. Peng, H. Makino, K. Inaba, H.J. Ko, K. Sumiyama, T. Yao, J. Magn. Magn. Mater., 213 (2000) 321.

[45] J.M.D. Coey, M. Venkatesan, C.B. Fitzgerald, Nat. Mater., 4 (2005) 173.

[46] H.L. Yan, X.L. Zhong, J.B. Wang, G.J. Huang, S.L. Ding, G.C. Zhou, Y.C. Zhou, Appl. Phys. Lett., 90 (2007) 082503.

[47] H. Hong, J. Sakai, N.T. Huong, N. Poirot, A. Ruyter, Phys. Rev. B, 72 (2005) 045336.

[48] Y. Liu, J. Yang, Q. Guan, L. Yang, Y. Zhang, Y. Wang, B. Feng, J. Cao, X. Liu, Y. Yang, M. Wei, J. Alloy. Compd., 486 (2009) 835.

[49] D.A. Schwartz, K.R. Kittilatved, D.R. Gamelin, Appl. Phys. Lett., 85 (2004) 1395.

[50] H. Wang, Y. Chen, H.B. Wang, C. Zhang, F.J. Yang, J.X. Duan, C.P. Yang, Y.M. Xu, M.J. Zhou, Q. Li, Appl. Phys. Lett., 90 (2007) 052505.

Table

Table 1

Sample	Measured at.%		
	Ni	Zn	O
ZnO	-	49.0 ± 3.4	51.0 ± 1.4
2 at.% (nominal Ni doped ZnO)	1.2 ± 0.1	45.9 ± 3.6	52.9 ± 1.2
4 at.% (nominal Ni doped ZnO)	2.6 ± 0.2	44.7 ± 3.5	52.7 ± 1.2
6 at.% (nominal Ni doped ZnO)	4.4 ± 0.1	43.5 ± 3.5	52.1 ± 1.3

Figure

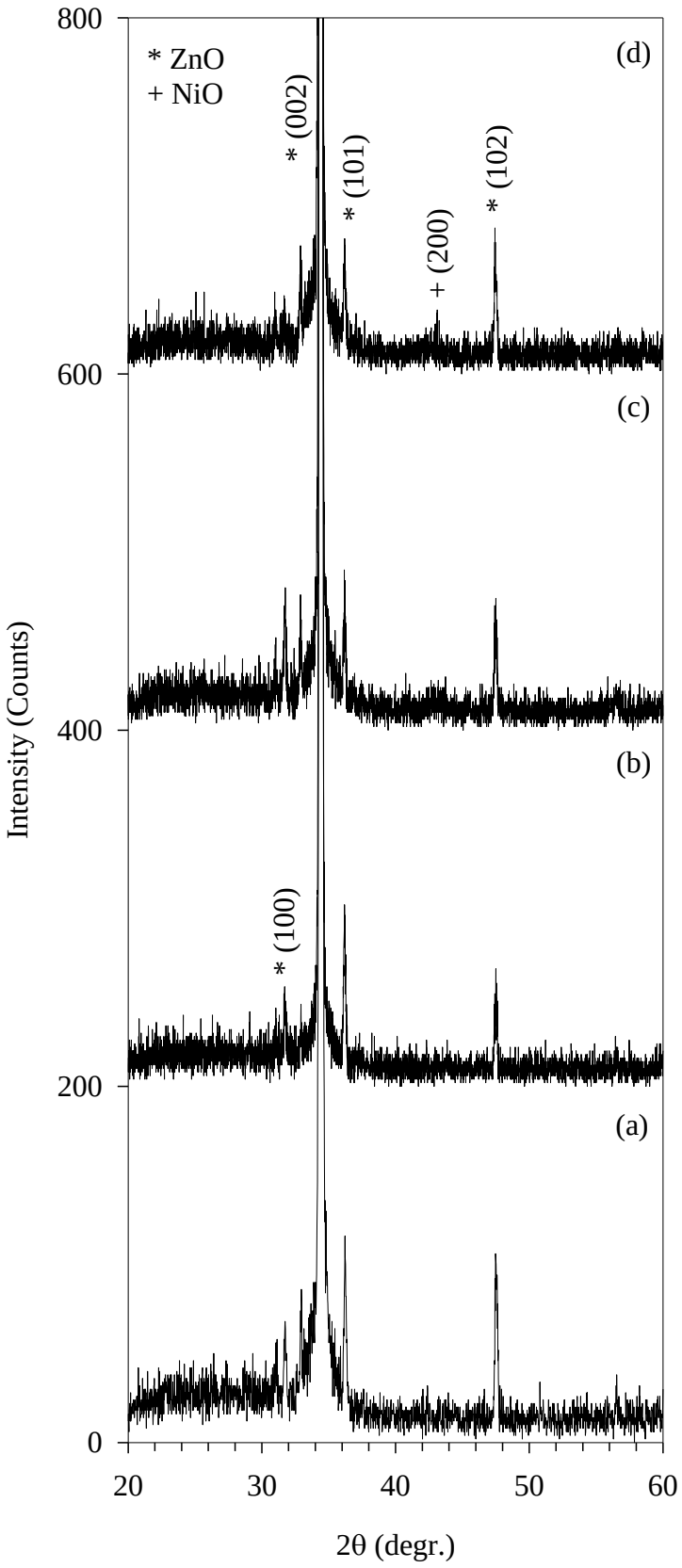
800
600
400
200
0
* ZnO
+ NiO
(d)
(c)
(b)
(a)
* (002)
* (101)
+ (200)
* (102)
* (100)
Intensity (Counts)
20
30
40
50
60
2θ (degr.)

Fig. 1

Figure

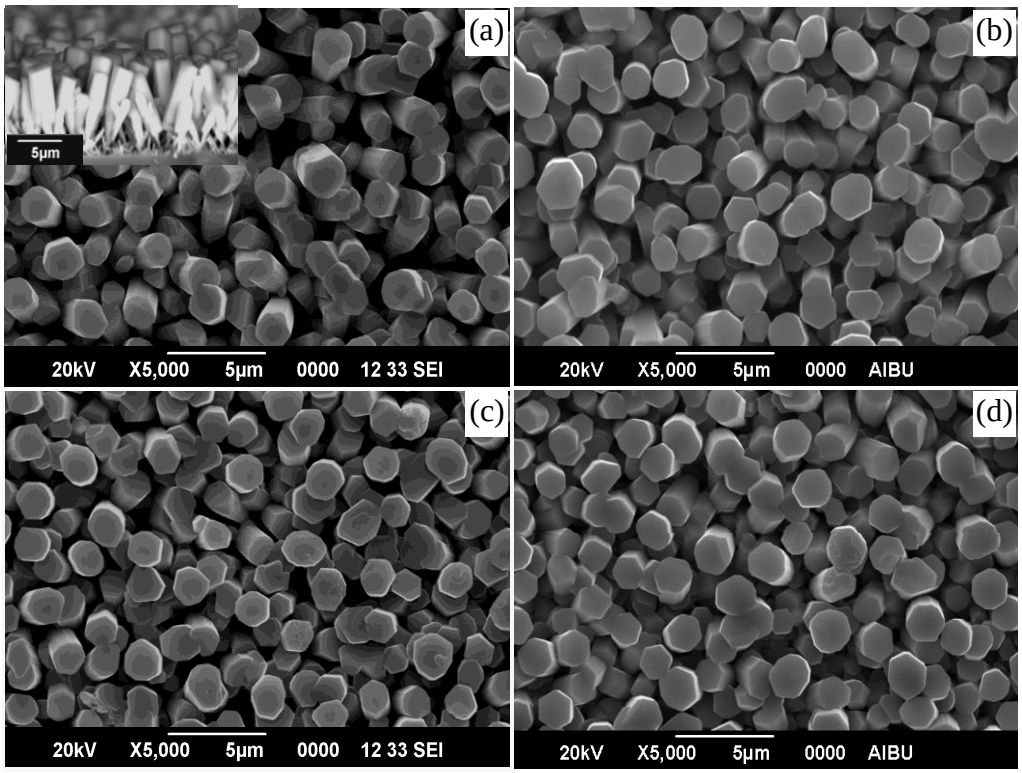
(a)
5μm
20kV X5,000 5μm 0000 12 33 SEI
(b)
20kV X5,000 5μm 0000 AIBU
(c)
20kV X5,000 5μm 0000 12 33 SEI
(d)
20kV X5,000 5μm 0000 AIBU

Fig. 2

Figure

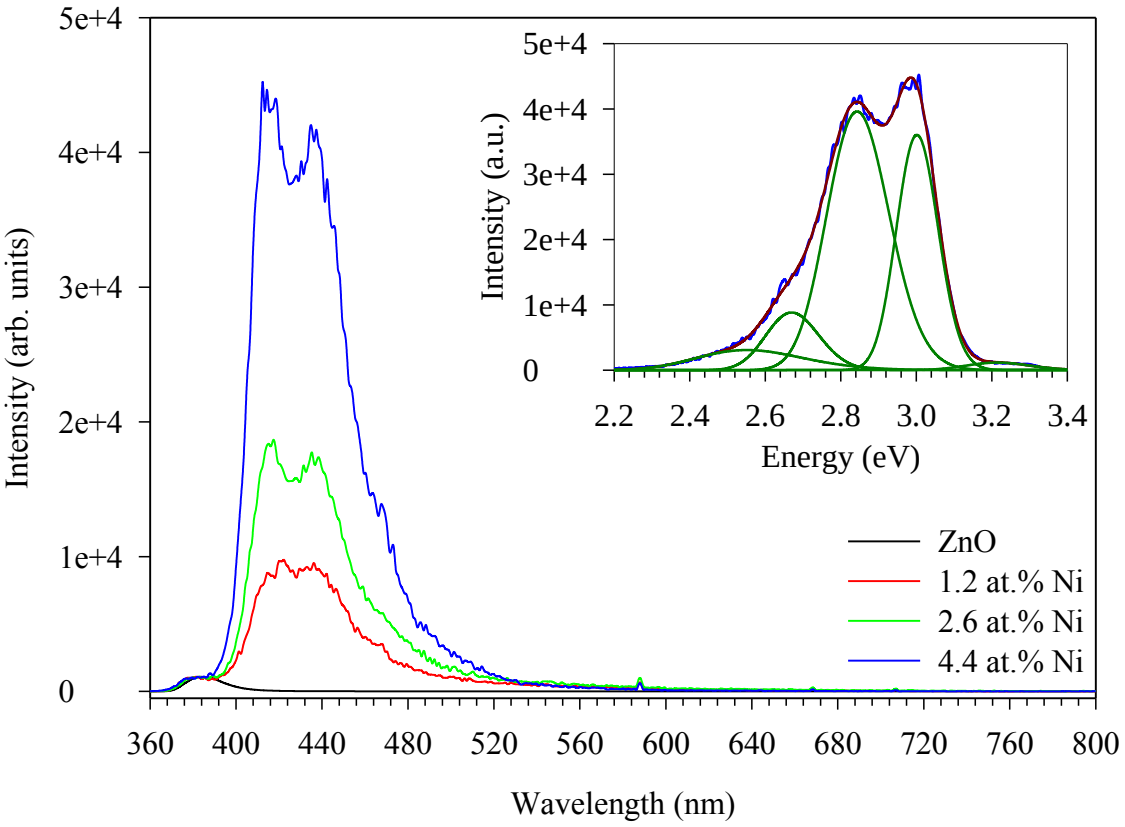
Intensity (arb. units)
5e+4
4e+4
3e+4
2e+4
1e+4
0
360
400
440
480
520
560
600
640
680
720
760
800
Wavelength (nm)
ZnO
1.2 at.% Ni
2.6 at.% Ni
4.4 at.% Ni
Intensity (a.u.)
5e+4
4e+4
3e+4
2e+4
1e+4
0
2.2
2.4
2.6
2.8
3.0
3.2
3.4
Energy (eV)

Fig. 3

Figure

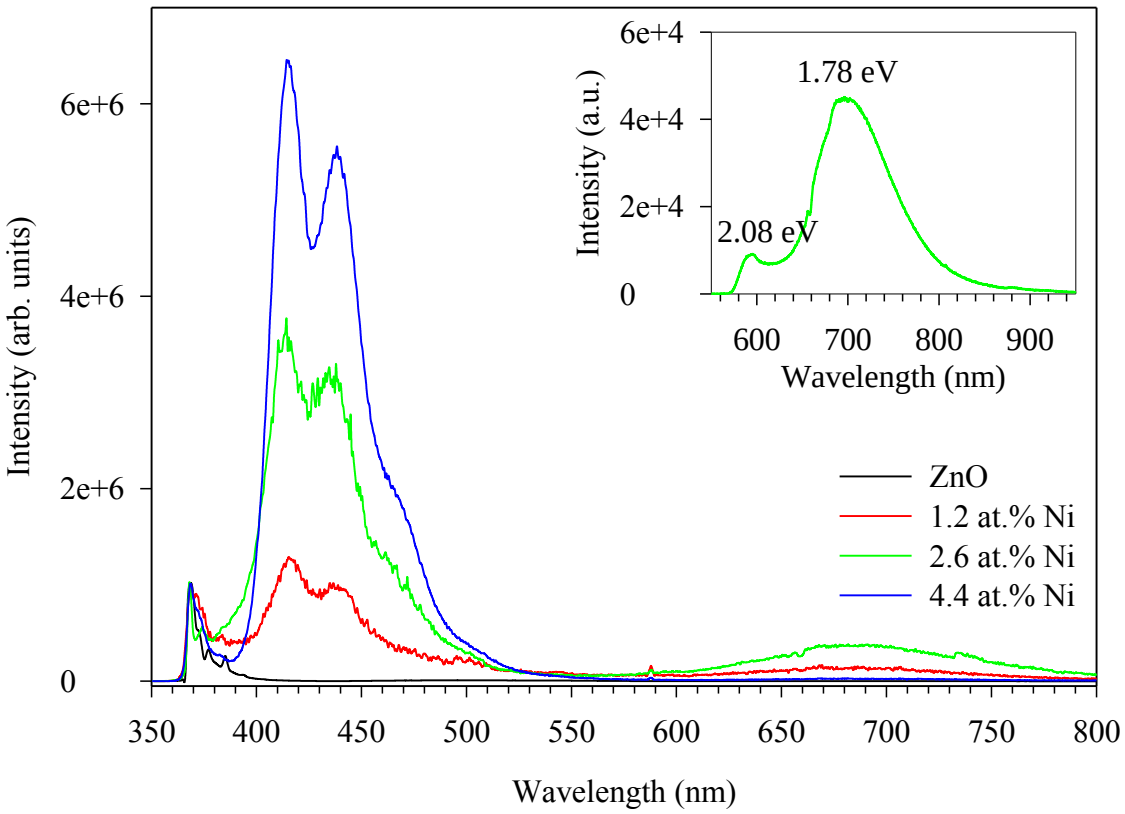
Intensity (arb. units)
6e+6
4e+6
2e+6
0
350
400
450
500
550
600
650
700
750
800
Wavelength (nm)
ZnO
1.2 at.% Ni
2.6 at.% Ni
4.4 at.% Ni
Intensity (a.u.)
6e+4
4e+4
2e+4
0
1.78 eV
2.08 eV
600
700
800
900
Wavelength (nm)

Fig. 4

Figure

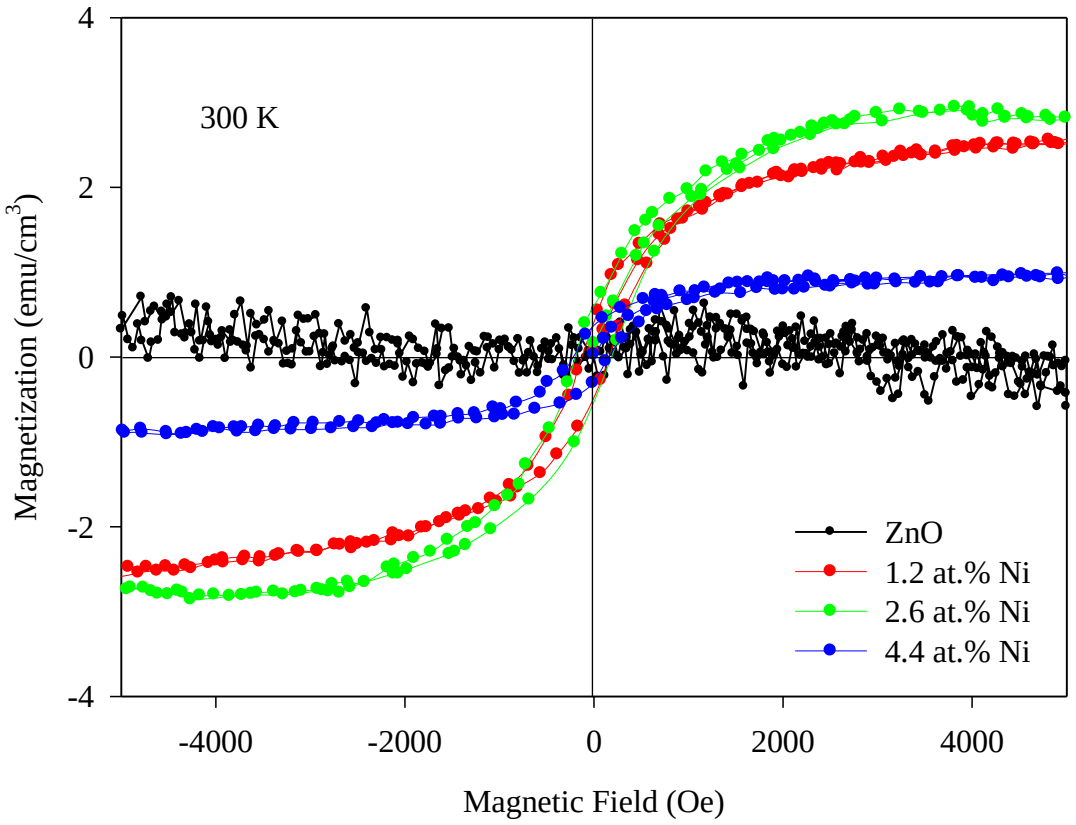
300 K
Magnetization (emu/cm3)
Magnetic Field (Oe)
4
2
0
-2
-4
-4000
-2000
0
2000
4000
ZnO
1.2 at.% Ni
2.6 at.% Ni
4.4 at.% Ni

Fig. 5

Figure

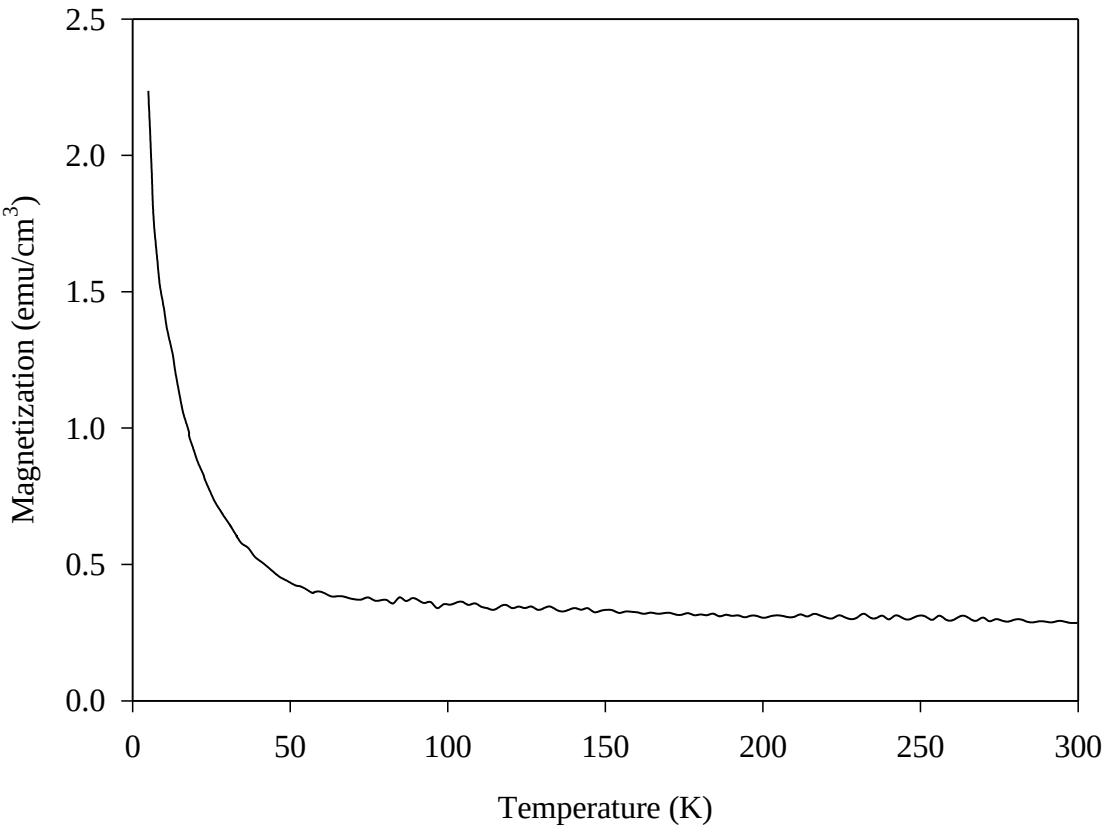
2.5
2.0
1.5
1.0
0.5
0.0
Magnetization (emu/cm3)
0
50
100
150
200
250
300
Temperature (K)

Fig. 6